PTEP

Prog. Theor. Exp. Phys. **2024**, 00000 (20 pages)
DOI: 10.1093/ptep/0000000000

Direct Reactions and Spectroscopy with Hydrogen Targets at the RIBF

Carlos A. Bertulani[1], Pieter Doornenbal[2], Alexandre Obertelli[3], and Tomohiro Uesaka[4]

[1]*Department of Physics and Astronomy, East Texas A&M University, Commerce, Texas 75429-3011, USA*
[2]*RIKEN Nishina Center, 2-1 Hirosawa, Wako, Saitama 351-0198, Japan*
[3]*Technische Universität Darmstadt, 64289 Darmstadt, Germany*
[2]*RIKEN Nishina Center, 2-1 Hirosawa, Wako, Saitama 351-0198, Japan*

The implementation of MINOS, a liquid-hydrogen target and vertex-tracking system, at the Radioactive Isotope Beam Factory (RIBF) of the RIKEN Nishina Center has led to numerous nuclear physics discoveries. In experiments involving rare-isotope beams at intermediate energies, MINOS was integrated with the DALI2$^+$ γ-ray spectrometer and other auxiliary devices. These were positioned in front of both the ZeroDegree Spectrometer and the SAMURAI magnetic spectrometers for the identification of ejectiles following quasi-free scattering direct reactions. Notable outcomes include the first spectroscopy of unstable doubly magic nucleus, investigations into multi-neutron decays, and the study of shell evolution along isotopic chains. These studies have significantly advanced our understanding of nuclear structure, as well as the mechanism of direct reactions with fast beams.

Simultaneously, these direct reactions enabled raising new physics questions and paved the way for next-generation experimental setups to address them. Through the combination of particle- and γ-spectroscopy with a broad range of nuclear reactions, new frontiers will be established in our understanding of nuclear structure and reaction mechanisms. Here, we review the past ten years of studies on direct reactions and spectroscopy of exotic nuclei with liquid-hydrogen targets at the RIBF and define a vision for the future.

Subject Index xxxx, xxx

1. Introduction

Atomic nuclei are few-body systems governed by the strong force and quantum mechanical laws that lead to a shell structure. The nuclear shell model, a cornerstone of nuclear physics, was developed to explain observations that atomic nuclei with certain "magic numbers" of protons or neutrons exhibit particular stability [1, 2]. In analogy to the arrangement of electrons in atomic orbitals, protons and neutrons (collectively called nucleons) occupy discrete energy levels or "shells", also constituting a direct fingerprint of the inter-nucleon many-body interactions. Isotopes featuring a complete shell filling for protons and/or neutrons (2, 8, 20, 28, 50, 82, 126) are called 'magic' and exhibit spherical shapes. They are more inert than their neighbors since their excitation requires more energy to promote nucleons above the energy gap to reach the next shell.

The nuclear shell model is founded on the idea that nucleons move independently within an average potential generated by all other nucleons. In the simplest calculations, this one-body potential can be approximated by using either a harmonic oscillator or a Woods-Saxon potential. A key aspect of the model is strong spin-orbit coupling, where the interaction between a nucleon's spin and its orbital motion leads to significant energy-level splitting, which helps explain the occurrence of magic numbers. Advances in theoretical models and experimental capabilities have enabled more precise tests of the shell model, particularly for nuclei far from stability, often referred to as "exotic nuclei."

However, magic numbers are not constant across the nuclear chart. In fact, the nuclear shell structure can change substantially with varying numbers of protons and neutrons, a process called shell evolution which reveals the intricate arrangement of nucleons governed by underlying forces. In certain regions, new shell closures or significant shell rearrangements have been observed or predicted, even in areas that are challenging to investigate experimentally. Moreover, changes in structure with respect to isospin can unveil new regions characterized by deformation. Nuclei near the neutron drip-line exhibit novel features, such as neutron halos and distinct ground-state clustering, including alpha or di-neutron clusters. Studying nuclei with a large neutron excess offers a unique opportunity to probe the nuclear equation of state (EOS) for neutron-rich matter, providing valuable insights for understanding neutron stars and neutron-star mergers, which are key drivers of heavy-element nucleosynthesis in the universe.

The spectroscopy of rare isotopes at intermediate energies, ranging from fifty to several hundred MeV/nucleon, has proven to be a powerful tool for deciphering their structure. However, a major constraint in exploring the nuclear landscape of short-lived nuclei lies in the available beam intensities, reachable luminosities, and the resolution of experimental measurements. To investigate the structure of the most neutron-rich nuclei systematically, a dedicated physics program, SEASTAR (Shell Evolution And Search for Two-plus energy At RIBF), was launched in 2013 at the RIBF at RIKEN, Japan. Since its establishment in 2007, this facility provides the world's most intens rare-isotope beams at intermediate energies. Hence, it was only natural to develop a new device, MINOS (Magic Numbers Off Stability) [3] dedicated to quasi-free scattering secondary reactions at the RIBF. MINOS consisted of a thick (up to 150 mm) liquid hydrogen target surrounded by a vertex tracker, thereby maximizing luminosity and resolution. Built at CEA, France, in the period 2010–2013, MINOS enabled the SEASTAR program and was employed at the RIBF for a multitude of extremely successful experiments from 2014 until 2017.

We present here a short introduction to direct reactions with fast beams, the RIBF, a summary of the MINOS working principle and associated detectors, and the physics addressed in quasi-free scattering experiments at intermediate energies.

2. Quasi-free Reactions

First theoretical studies of (p,2p) reactions and nucleon-nucleon quasi-free scattering (QFS) date back to 1958 [4, 5]. Since then, most experimental analyses of QFS employ the Distorted Wave Born Approximation (DWBA), often referred to as the Impulse Approximation. This formalism and comparison to experiments has been thoroughly reviewed in Ref. [6]. In the DWBA framework, nuclear excitations during the process are treated to first order, while the scattering waves for nucleon-nucleus elastic scattering in both the incoming and outgoing

channels are handled exactly. This formalism leads to a differential cross section expressed as [4]

$$\frac{d^6\sigma}{dE_p d^2\Omega_p dE_N d^2\Omega_N} = \frac{S(lj)}{2(2J_A+1)}\mathcal{K}\frac{d\sigma_{pN}^{fr}}{d\Omega}\sum_{\mu}|\mathcal{T}_{pN}(\mu)|^2\delta(E_p+E_N+E_{A-1}-E_A+E_0), \tag{1}$$

where the sum involves the spin magnetic quantum numbers of the incident proton (index 0), the target nucleus (A), the final proton (p), the struck nucleon (N), and the residual nucleus ($A-1$). For single-particle states, a simpler notation jlm is often used for the angular momentum quantum numbers of the ejected nucleon. $S(lj)$ is the spectroscopic factor for the removed nucleon from the orbital labeled by the angular quantum numbers l and j. $\mathcal{K}$ is a kinematical factor depending on initial and final energies and angles. Here, E_0 is the beam energy. $d\sigma_{pN}^{fr}/d\Omega$ is the free proton-nucleon (N) cross section. The transition matrix $\mathcal{T}_{pN}$ depends on the initial and final wavefunctions of the particles, including the intrinsic wavefunctions of the nuclei and is averaged over initial spins. $\mathcal{T}_{pN}$ has been treated theoretically using diverse degrees of approximations and corrections and have been reported in a large number of publications including extensions of the formalism to describe reactions with polarized beams/targets, as well as modifications to allow the treatment of (p,pα) and (α, 2α) reactions (see, e.g., Refs. [7–17]). Experiments in the 60s and the following decades using protons beams around 100-200 MeV incident on stable targets, guided by theory constructed around Eq. (1), have provided invaluable nuclear structure information. Theory support lead to the development of computer codes such as *threedee* [7], used up to now in the experimental analyses of energy and angular distributions [18], and *PIKOE [19]*. Among the several inputs of the DWBA formalism, the most uncertain one is the optical potential.

Recently, an independent formalism was developed to describe momentum distributions and total cross sections using eikonal waves for the incoming proton up to the collision point z within the nucleus, and eikonal waves for the outgoing nucleons from z to infinity [20]. The advantage of the method are the rather simple equations obtained. The longitudinal and transverse momentum distribution of the recoiled nucleus are given by

$$\frac{d\sigma}{dQ_z} = \frac{S(lj)}{2j+1}\left(\frac{d\sigma_{pN}}{d\Omega}\right)_{Q_z}\sum_m \mathcal{C}_{lm}\int_0^\infty db\, b\,|\mathcal{S}(b,Q_z)|^2\left|\int_{-\infty}^{\infty}dz e^{-iQ_z z}\frac{u_{lj}(r)}{r}P_{lm}(\cos\vartheta)\right|^2, \tag{2}$$

$$\frac{d\sigma}{Q_t dQ_t} = \frac{S(lj)}{2j+1}\left(\frac{d\sigma_{pN}}{d\Omega}\right)_{Q_t}\sum_m \mathcal{C}_{lm}\int_{-\infty}^{\infty}dz\left|\int_0^\infty db\mathcal{S}(b,Q_t)\frac{u_{lj}(r)}{r}J_m(Q_t b)P_{lm}(\cos\vartheta)\right|^2, \tag{3}$$

where the free pN cross sections $d\sigma_{pN}/d\Omega$ and the eikonal S-matrices $\mathcal{S}$ are restricted by the respective momenta Q_z or Q_t. In these expressions, J_m is the cylindrical Bessel functions, and $P_{lm}(\cos\vartheta)$ are the associated Legendre polynomials, with $\cos\vartheta = z/\sqrt{b^2+z^2}$ and $\mathcal{C}_{lm} = (2l+1)(l-m)!/[4\pi(l+m)!]$. The radial single-particle wavefunction for the removed nucleon is denoted by u_{lj}. It is the radial part of the overlap function $I(\mathbf{r}) = \langle\Psi_i^{A-1}|\psi(\mathbf{r})|\Psi_{g.s}^A\rangle$, where $|\Psi_{g.s.}^A\rangle$ and $|\Psi_i^{A-1}\rangle$ respectively, denote the (many-body) wave functions for the projectile and the residual fragment in its ith excited state. The operator $\psi(\mathbf{r})$ removes a nucleon at position $\mathbf{r}$.

The total cross section is

$$\sigma = S(lj)\frac{2\pi}{2j+1}\sum_m \left\langle \frac{d\sigma_{pN}}{d\Omega} \right\rangle |\mathcal{C}_{lm}|^2 \int_0^\infty db\, b\, |\langle \mathcal{S}(b) \rangle|^2 \int_{-\infty}^\infty dz \left| \frac{u_{lj}(r)}{r} P_{lm}(b,z) \right|^2 . \quad (4)$$

The brackets $\langle\rangle$ represent an average that can be done by a sampling of the differential cross sections and S-matrices for several final momenta $\mathbf{k}_p$ and $\mathbf{k}_N$ with the constraint set by conservation of energy and momentum of all particles involved. The information on the reaction mechanism is encoded in the S-matrices $\mathcal{S}$ that are usually obtained in terms of the nucleon-nucleon cross sections. They account for absorption which arises when the quasi-free scattering is followed by subsequent nucleon-nucleon collisions. Pauli blocking, relativistic, in-medium nucleon-nucleon scattering, and Fermi motion corrections can be easily incorporated. For more details we refer to Ref. [20].

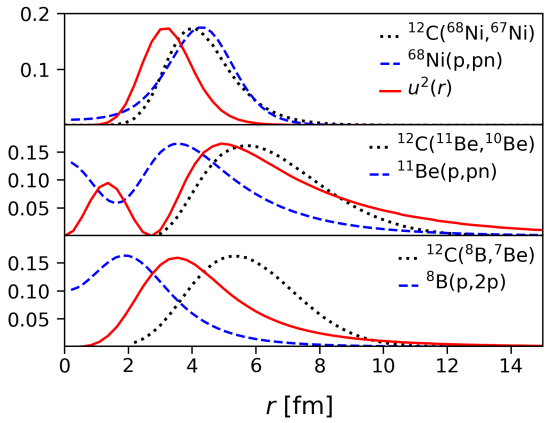

Fig. 1 *Upper panel:* The dashed curve shows the probability for removal of a neutron in the reaction ^{12}C(^{68}Ni,^{67}Ni) at 500 MeV/nucleon as a function of the distance to the c.m. of ^{68}Ni. The dotted curve represents the removal probability in a ^{68}Ni(p,pn) reaction at the same energy. Both curves are the normalized integrand as a function of the impact parameter of Eq. 4. For comparison the square of the radial wave function $u(r)$ is shown (solid red curve). *Middle:* Same, but for the reactions ^{12}C(^{11}Be,^{10}Be) and ^{11}Be(p,pn) at 500 MeV/nucleon. *Lower:* Same, but for the reactions ^{12}C(^{8}B,^{7}Be) and ^{8}B(p,2p) at 500 MeV/nucleon.

With the advancement of new detectors in newly constructed radioactive beam facilities, proton targets were used to infer (p,2p) observables in inverse kinematics. It took some time for the first exclusively complete and inverse kinematics experiment to be achieved using a ^{12}C beam at an energy of 400 MeV/nucleon as a benchmark [21]. In the subsequent years a large number of experiments with complete kinematics were performed, specially using light neutron-rich nuclei. Some attention was paid to compare (p,pN) spectroscopic information on nuclei far from the stability with those obtained with heavy ion knockout reactions, as described in the review of Ref. [18]. Perhaps the most spectacular application of the QFS formalism was the discovery of the tetraneutron resonance using the ^{8}He(p,pα) reaction [22].

One of the advantages of using eikonal distorted waves for the description of (p,2p) and heavy ion knockout reactions is the interpretation of the transverse component of the eikonal wave as classical impact parameters. One can study how the impact parameter is sampled in both reactions. This is shown in Fig. 1 and explained in the caption. It is assumed a neutron removed from the $0f_{7/2}$ orbital in ^{68}Ni, bound by 15.68 MeV, a neutron in the $1s_{1/2}$ orbital in ^{11}Be, bound by 0.54 MeV and a proton in the $0p_{3/2}$ orbital in ^{8}B, bound by 0.14 MeV. For ^{68}Ni the removal cross sections for both knockout and (p,pn) reactions probe mostly

the surface part of the wave function because in both cases the absorption is very strong for small impact parameters. For proton or neutron removal from even deeper bound states, with a concentration of the wave function closer to the origin, both reaction mechanisms will probe an even smaller part of the wave function tail. In the case of light nuclei such as ^{11}Be or ^{8}B, the heavy ion knockout reaction is more constrained to the surface of the nucleus, beyond the orbital maximum density. On the other hand, the (p,pN) reaction has a much larger probability of accessing information on the inner part of the wave function, as seen by the dashed curve. Recent works [23, 24] have shown that not only the tail of the overlap functions, but also their internal part is assessed in both reaction heavy ion knockout and (p,pN) reactions. Both parts of the wavefunction are crucial to yield accurately determined spectroscopic information. In view of the recent advances in experimental facilities and detection techniques, it is suggested that heavy-ion knockout and (p,pN) reactions be analyzed using a consistent many-body model, because they are a formidable tool to extend our knowledge in nuclear spectroscopy only when many-body correlations are considered in the analysis.

3. The Radioactive Isotope Beam Factory

The RIBF [25], located within the Wako Campus of RIKEN in Japan, is a state-of-the-art accelerator complex designed for advanced studies in low-energy nuclear physics. One of its key assets is the production and study of atomic nuclei far from stability. It features multiple coupled cyclotrons, including the one with the world's highest total beam energy, the superconducting ring Cyclotron (SRC) [26], which can accelerate stable isotopes up to 345 MeV/nucleon. The BigRIPS fragment separator [27] is instrumental in isolating and purifying the rare isotopes generated by fragmentation or fission of the primary beam.

3.1. Accelerator and Primary Beam Intensities

The RIBF accelerator complex features two parts, a first-generation facility in operation since 1986, and the new facility delivering beams since 2007, following the commissioning of three ring cyclotrons: The fixed-frequency Ring Cyclotron (fRC), the Intermediate-stage Ring Cyclotron (IRC), and the SRC. These three cyclotrons enhance the energies of beams accelerated by the RIKEN Ring Cyclotron (RRC) from the old facility. Prior to entering the four coupled cyclotrons, beams are injected by either the AVF, the RIKEN Linear ACcelerator (RILAC), or the RILAC2. At present, the latter is the main injector for most rare isotope experiments and is equipped with a 28-GHz superconducting electron-cyclotron-resonance ion source (SC-ECRIS). A key feature of the RIBF accelerator complex is its capability to accelerate all ions from hydrogen to uranium up to 70% of the speed of light, 345 MeV/nucleon. Two charge strippers belong to the acceleration scheme: A helium gas stripper at the RRC exit (E=11 MeV/nucleon) and a rotating graphite-sheet stripper between fRC and IRC (E=50 MeV/nucleon). Both are employed for the acceleration of heavy beams, such as ^{124}Xe or ^{238}U, while lighter beams (e.g. ^{70}Zn or ^{78}Kr) require only the second charge stripper. In total, three acceleration schemes exist: The fixed energy mode (for Zn, Kr, Xe, and U isotopes), the variable energy mode (for Ca), and the AVF injection mode (for light ions). A diagram of these three schemes together with the injectors and the four cyclotrons is provided in Fig. 2.

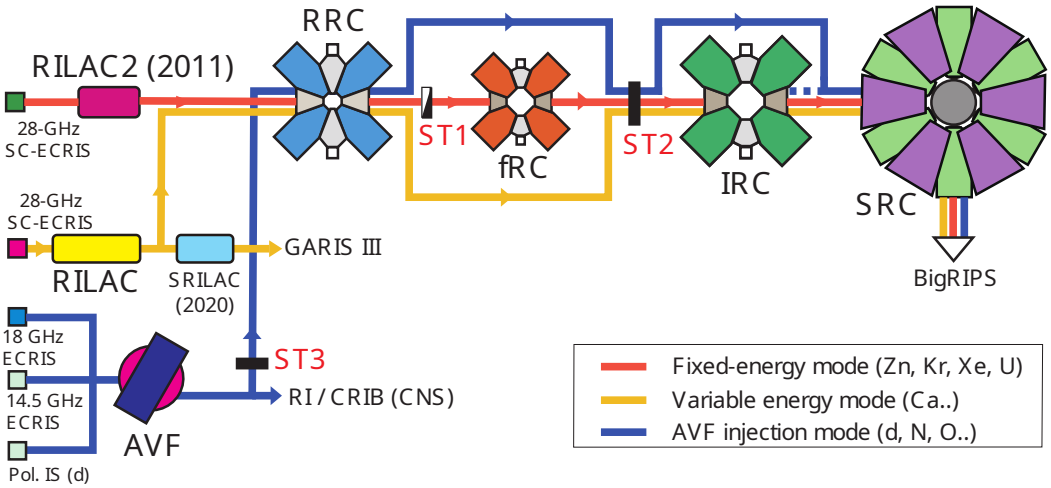

Fig. 2 The three acceleration schemes currently employed at the RIBF. Depicted are the three injectors with their respective ion sources, the four cyclotrons, and the different acceleration schemes going to the BigRIPS [27] fragment separator. See text for details. Adopted from Ref. [28].

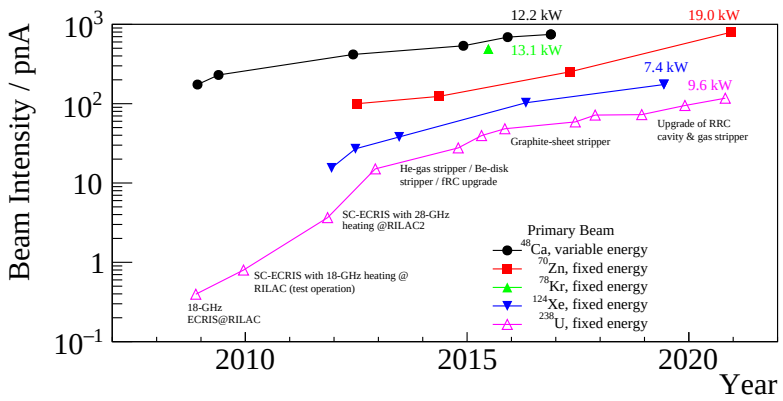

Fig. 3 Beam power progression over time at the exit of the SRC since the inception of the RIBF. Maximum beam power as well major development steps are indicated. Beam intensity values of the figure have been adopted from Ref. [29].

Figure 3 illustrates the progression of maximum beam intensity for ion beams accelerated at RIBF. Thanks to continuous developments, such as the new 28 GHZ ion source SC-ECRIS [30], the injector RILAC2 [31], a novel helium-gas stripper [32], implementation of a graphite-sheet stripper, as well as an upgrade of the RRC cavities [33], the ^{238}U primary beam intensity has now reached 117 pnA, corresponding to a power of almost 10 kW. With the first charge stripper no longer being required for medium mass isotopes, the beam power reached 19 and 13 kW for ^{70}Zn and ^{78}Kr, respectively.

Currently, an upgrade plan of the RIBF is being devised [28]. At its center, two charge stripper rings (CSR) will replace the current strippers. These two rings will recycle the beam until the desired charge state is reached. Thereby, the stripping efficiencies for ^{238}U beam of ≈20% and ≈25% will increase to ≈80% for both CSR. Together with a more powerful ion source, an intensity of 2000 pnA (160 KW), i.e., an increase of a factor 20, is expected in the future.

3.2. Secondary Beams from BigRIPS

Secondary beams are produced, selected, and separated by the BigRIPS fragment separator [27] by striking the primary beams on a thick stationary Be reaction target located at the focal point F0 in Fig. 4. Key features of BigRIPS include its large acceptance and high transmission for in-flight fragmentation and fission products. It consists of six dipoles with a bending angle of 30° and fourteen superconducting quadrupole triplets (STQ) with a total length of 78 meters, and is operated as a two-stage separator. In the first stage from F0 to F2, the ions of interest are selected and separated via the $B\rho - \Delta E - B\rho$ method by placing a wedge-shaped degrader in-between the first two dipoles, allowing for a purification of the secondary beams. However, completely pure secondary beams cannot be achieved. Accordingly, tagged secondary beams identified event-by-event must be obtained in a second stage. From F3 to F7 the $B\rho - \Delta E -$TOF method [34] ensures this by beam-line detectors. Several options for particle identification exist, but typically position-sensitive parallel plate avalanche counters (PPACs) [35] are placed at the focal points to reconstruct $B\rho$, particularly the dispersive focal point F5, while plastic detectors measure the time of flight (TOF) from F3 to F7, and a multi-sampling ionization chamber (MUSIC) [36] measures ΔE at F7. Basic parameters of BigRIPS, when operated in the "standard" mode, include angular acceptances of ±40 mrad horizontally, ±50 mrad vertically, a momentum acceptance of ±3 %, a momentum dispersion of +31.7 mm / % at mid-focus, and a momentum resolution of $p/\delta p = 3420$ (σ) [27].

Following separation and identification, secondary beam energies range between 150 and 300 MeV/nucleon and are guided to the specific experimental setup, for quasi-free reactions with the MINOS system and subsequent in-flight γ-ray detection with DALI2$^+$ [37], located either at the F13 focus of SAMURAI [38] (Superconducting Analyser for MUlti particles from RAdio Isotope beams) or the F8 focus of the ZeroDegree spectrometer [27].

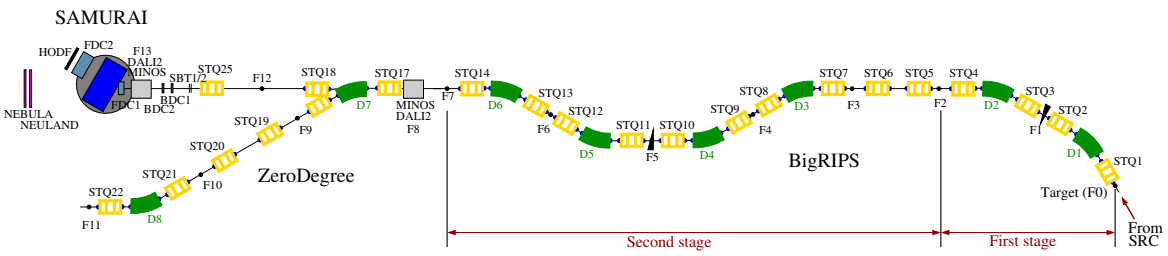

Fig. 4 Layout of BigRIPS, Zerodegree, and SAMURAI spectrometers (not to scale). The six dipoles of BigRIPS, spanning from F0 to F7, and the two dipoles of ZeroDegree, spanning from F8 to F11, are shown in green, while STQs are depicted in yellow, and SAMURAI in blue. MINOS and DALI2 detect quasi-free scattering and γ ray events at F8 or F13, respectively, for ZeroDegree or SAMURAI experiments. See text for details. NEBULA and NeuLAND detect neutrons of unbound excited states. A detailed description of the SAMURAI setup can also be found in Ref. [39] within this series. The Figure was adapted from Ref. [40].

3.3. SAMURAI and Associated Detector Systems

SAMURAI constitutes a large acceptance spectrometer for kinematically complete measurements, allowing for invariant-mass spectroscopy of particle-unbound excited states of rare isotopes. At its core, a large rotatable superconducting dipole magnet provides a large field integral of up to 7.1 Tm, a large gap of 0.88 m, and a large opening angle of ±175 mrad horizontally and ±87 mrad vertically, respectively. Only this large opening angle allows for efficient invariant-mass spectroscopy, yet challenges particle identification behind the reaction target.

In a typical experiment, a rotation of 30° enables maximum neutron detection efficiency. Upstream the reaction target, the beam's impact point is derived from two beam drift chambers (BDC1 and BDC2). Downstream, two forward drift chambers (FDC1 and FDC2) are placed in front and behind the SAMURAI magnet to extract the magnetic rigidity. A set of two plastic scintillators (SBT1 and SBT2) upstream the reaction target and a hodoscope for fragments (HODF), composed of 16 modules of each 100 mm width, behind the FDC2 measure the TOF needed to reconstruct the velocity. The flight path between the SBT1/2 and the HODF is about 13 m. For light rare isotopes up to element number $Z \approx 20$, the HODF and SBT provide sufficient energy-loss resolution to determine the element number in front and behind the reaction target, while heavier charge distributions can be obtained with an ion chamber (ICB or ICF) placed in front and/or behind the reaction target.

Two large-acceptance plastic scintillator arrays detect neutron emission of unbound excited states, the NeuLAND (New Large-Area Neutron Detector) demonstrator [41] and NEBULA (NEutron-detection system for Breakup of Unstable-Nuclei with Large Acceptance) [38, 42]. The NeuLAND demonstrator is part of the next-generation neutron detector for the R3B setup at FAIR that will constitute 3000 individual submodules with a size of 5×5×250 cm^3 arranged in 30 layers. During its stay at the RIBF from 2014 to 2017, the NeuLAND demonstrator was composed of 400 of these submodules in eight layers. Conversely, NEBULA consisted of 120 modules of 12×12×180 cm^3 in two layers. To enable sufficient momentum resolution, they were placed ≈12 m and ≈15 m downstream the reaction target.

3.4. The ZeroDegree Spectrometer

The ZeroDegree spectrometer consists of two dipoles, bent 30° against each other to form zero degree, and six STQs. To obtain particle identification of the reaction products, the $B\rho - \Delta E -$TOF method is employed. The beam line detectors are the same type as for BigRIPS and the dispersive focal points F9 and F10 are located in-between the two dipoles to provide the $B\rho$ information. For the quasi-free reactions experiments, ZeroDegree was operated in the Large Acceptance Achromatic mode (LAA mode), which featured an angular acceptances of ±45 mrad horizontally, ±30 mrad vertically, a momentum acceptance of ±3 %, and a momentum resolution of 1240 (σ) with a total length of 36.5 m [27].

3.5. DALI2

The Detector Array for Low Intensity radiation, DALI2 [37], consists of an assembly of large-volume NaI(Tl) detectors, which are closely packed around the reaction target to maximize efficiency, keeping the opening angle of each detector at a moderate level of around $\Delta\vartheta_\gamma \approx 7°$. As the γ rays are detected in-flight, a Doppler correction must be carried out. With an

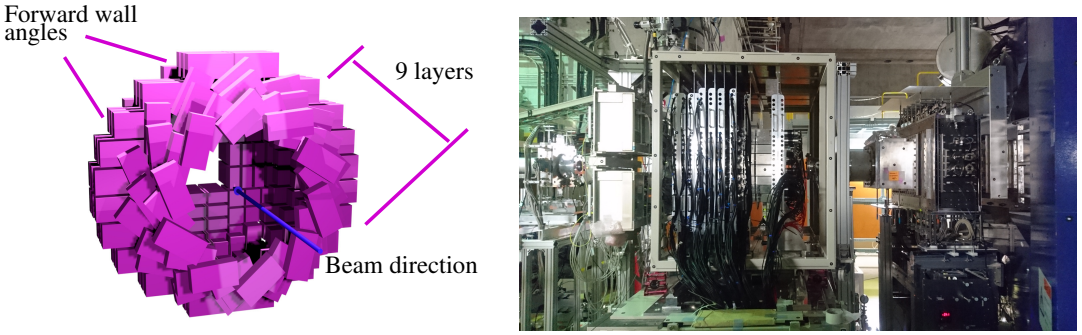

Fig. 5 (Left) Conceptual drawing of DALI2 with 9 layers perpendicular to the beam direction and the forward wall. (Right) Photograph of DALI2$^+$ and MINOS installed in front of the SAMURAI spectrometer.

intrinsic resolution of ≈ 6% at 1.33 MeV, due to the opening angles this results in energy resolutions of ≈10–11 % full-width at half maximum (FWHM) for 1 MeV γ rays emitted at secondary beam energies in the range 100–250 MeV/nucleon. The obtained full-energy peak (FEP) efficiency depends on the applied add-back algorithm. Typically, energies recorded in detectors with weighted centers within 10 to 15 cm are added back, the latter resulting in an FEP efficiency of ≈34 %. Further details on the performance of DALI2 can also be found in Ref. [43].

Over time, DALI2 received several upgrades. Experiments were carried out with 186 NaI(Tl) from 2010 – 2016. This value was augmented to 226 detectors in 2017 for the present DALI2$^+$ configuration [44], for which the detector arrangement allowed for a more evenly intensity distribution for γ rays emitted from the MINOS target at a velocity of $\beta = 0.6$. DALI2$^+$ consists of 10 layers. Counting from downstream to upstream, the first nine layers are arranged in rings perpendicular to the beam with 162 detectors, while the last layer forms a wall of 64 detectors placed parallel to the beam, as Fig. 5 shows. Distances from the detectors' geometrical centers to the target center vary between ≈ 300 to ≈ 500 mm.

Three different detector types are employed: 46 long crystals from SCIONIX with dimensions of 40×80×160mm^3, 92 long crystals from SAINT-GOBAIN with dimensions of 45×80×160mm^3, and 88 "DALI1"-type shorter detectors with dimensions of 60×60×120mm^3. The latter are a mixture of detectors manufactured by BICRON, SAINT-GOBAIN, SCIONIX, and LUXIUM. It is noteworthy that in 2017, the array was replaced by 60 "DALI1"-type detectors (from SAINT-GOBAIN) from the University of Hong Kong (HKU). In 2023, a further detector replacement took place: 10 detectors of the long SAINT-GOBAIN and 10 "DALI1"-type detectors from LUXIUM, both types owned by ATOMKI, as well as a further 10 "DALI1"-type detectors from SCIONIX, owned by HKU.

3.6. MINOS

MINOS uses nucleon-removal from very exotic nuclei on a very thick liquid hydrogen target combined to a proton tracker that aims at measuring, on an event-by-event basis, the reaction-vertex position in the target.

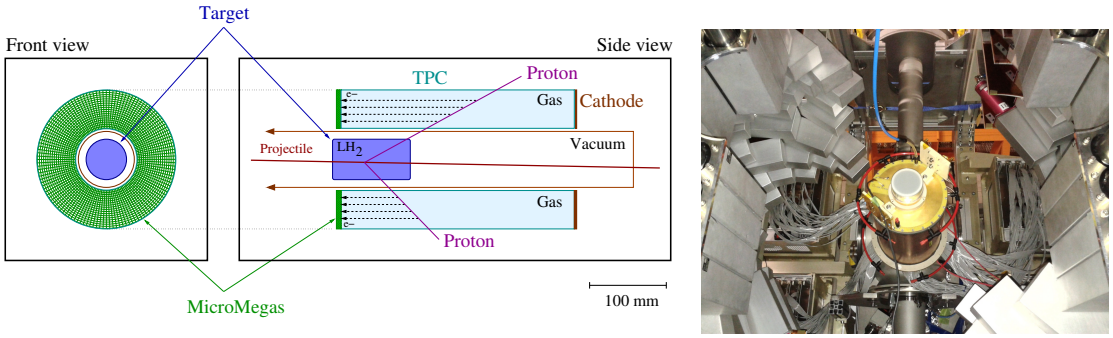

Fig. 6 (Left) Operational scheme of the MINOS device. Adopted from Ref. [40]. (Right) Photograph of the MINOS device inside DALI2. Note that DALI2 has been opened. During experiments, the left and right side are moved closer to MINOS.

A cut view of the device is shown in Fig. 6. Measurement of the vertex position with a 5 mm resolution (FWHM) allows for the use of targets of hundreds of millimeters with improved detection sensitivity, i.e., by improving the Doppler correction in case of in-beam γ-ray spectroscopy or the scattering angle and energy of recoil charged particles in the case of missing mass spectroscopy.

For a target of such thickness, it's crucial to minimize, or at least control, the probability of a "second interaction" within the target, as the knockout fragment must be identified after passing through the target. At RIBF incident energies, a typical length of 150 mm meets this requirement when particle identification in front and behind MINOS ensure a single quasi-free (p, pn) or $(p, 2p)$ reaction. This thickness enhances detection sensitivity by up to an order of magnitude compared to experiments using solid heavy-ion targets due to higher luminosity per unit of energy loss of the secondary beam and reduced $\Delta\vartheta_\gamma$ and $\Delta\beta_\gamma$ due to vertex reconstruction. MINOS was completed and validated at HIMAC and RIKEN in 2013, and has been in use at the RIBF from 2014 to 2017 for experiments. The MINOS support structure was designed to integrate with DALI2$^+$ and was compatible with both the ZeroDegree and SAMURAI experimental areas. Depending on the beam time schedule, experiments could be easily set-up at either location.

The MINOS device, depicted in Fig. 6, consisted of a thick liquid cylindrical hydrogen target [45, 46] (possible target lengths ranging from 50 to 200 mm) and was surrounded by an annular Time Projection Chamber (TPC) equipped with a Micromegas [47, 48] amplification stage above a segmented pad plane to track recoil protons from quasi-free scattering reactions and to reconstruct the vertex position inside the target. During experiments, beam particles pass through the liquid hydrogen target, where a knockout reaction may occur. The heavy fragment is scattered at a small angle from the original beam direction and is identified downstream. The recoiling protons are ejected at larger angles, and in most cases, at least one of the two intersects the TPC surrounding the target. For $(p, 2p)$ reactions, the probability of detecting at least one proton exceeds 90%, while the efficiency for detecting both protons reaches 60% due to the large solid-angle coverage of the TPC around the target. As charged particles traverse the TPC, they ionize the gas, which in the experiments comprised a mixture of Ar (82%), isobutane (3%) and CF_4 (15%). The ionized electrons then drift towards the

anode, or Micromegas detection plane, under an electric field of approximately 300 V/cm. The tracks recorded in the TPC are exclusively straight lines, as no magnetic field is applied, and the charge deposition along the track is uniform for energetic protons. A specialized tracking algorithm filters out delta electrons and fits the tracks using Hough transforms within a cylindrical geometry [49].

The signals generated by the detector are processed and read by specialized readout electronics [50], which are equipped with advanced AGET chips. The signals are read out using dedicated Feminos cards [51]. These cards are all synchronized to a common clock and trigger via a Trigger Clock Module card. The experiments operate in a common dead-time mode, with a trigger rate not exceeding 1 kHz. For more detailed information on MINOS, see Ref. [3].

4. Nuclear Structure Challenges

Contemporary research in nuclear structure focuses on elucidating the interactions within nuclei, especially concerning the exotic nuclei that lie far from stability. This requires a comprehensive analysis of the intricate interactions among nucleons from various perspectives, including macroscopic, microscopic, and *ab-initio* approaches. Such an understanding facilitates the characterization of a wide range of phenomena, such as the appearance and vanishing of magic numbers, shape transformations and coexistence, clustering and halo formation, and the boundaries of nuclear stability.

MINOS explored these phenomena through quasi-free scattering. The subsequent sections offer concise explanations of the subjects and link them to the given summaries.

4.1. Magic Numbers and Islands of Inversion

For a long time, researchers have embarked on a mission to identify and thoroughly explore nuclei possessing magic neutron and proton numbers beyond the valley of stability. Doubly magic radioactive nuclei provide a distinctive probe to examine our understanding of the nuclear shell model in nuclei with significant isospin, where correlations like pairing or deformation are minimized. Away from the valley of stability, new magic numbers may emerge, whereas the "standard" ones may disappear. One of the most prominent examples of such a vanishing magic number is the neutron gap between the $0d_{5/2}$, $1s_{1/2}$, and $0d_{3/2}$ orbitals in the *sd* shell and the $0f_{7/2}$ and $1p_{3/2}$ orbitals from the adjacent *pf* shell, forming the magic number $N = 20$. The mass anomalies of ^{31,32}Na revealed that they were more tightly bound than expected [52]. Hartree-Fock calculations suggested that neutrons fill the $0f_{7/2}$ shell before the *sd* shell [53], leading to the erosion of the $N = 20$ shell. Measurements of $E(2_1^+)$ in ^{32} Mg [54] and its associated $B(E2)\uparrow$ [55] further confirmed the notion of the shell erosion, accompanied by an increase in deformation in this region of the nuclear chart, also termed "Island of Inversion" [56]. Further research manifests the merging of the $N = 20$ and $N = 28$ shell erosions [57] into a broad Island of Deformation [58].

Shell evolution refers to this structural transformation that occurs as the number of protons or neutrons changes. Building on initial in-beam γ experiments conducted at the RIBF (see, for example, Refs. [60–62]), the SEASTAR project was created to systematically investigate this phenomenon across isotopes ranging from calcium to zirconium by measuring their $E(2_1^+)$. Here, the isotopic chain of calcium isotopes is particularly intriguing. Following doubly magic stable isotopes ^{40}Ca and ^{48}Ca, ^{52,54}Ca exhibit relatively high $E(2_1^+)$. For

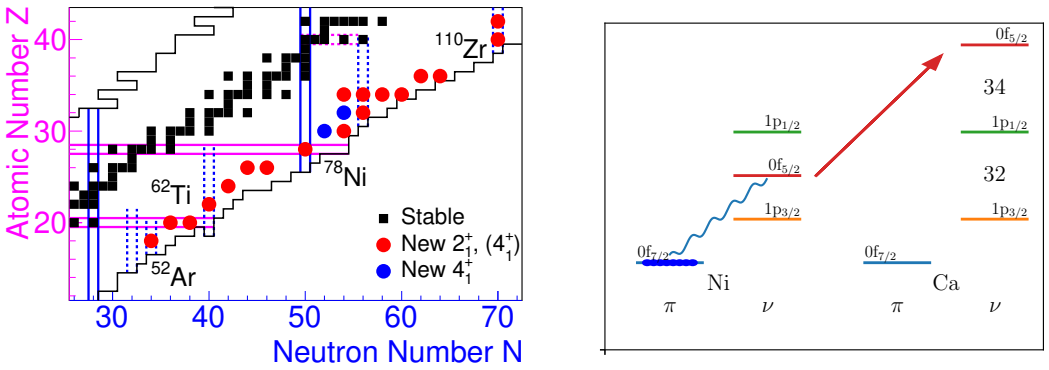

Fig. 7 (Left) nuclear chart showing the newly observed $E(2_1^+)$ and $E(4_1^+)$ with SEASTAR. (Right) schematic of the interaction between protons in the $0f_{7/2}$ and neutrons in the $0f_{5/2}$ shell producing the $N = 32, 34$ magic numbers in the calcium isotopic chain. The figure was adapted from Ref. [59].

these isotopes, new neutron shell closures at $N = 32$ and $N = 34$ are identified. The marked spherical shell gaps observed in these neutron numbers for calcium isotopes are linked to the attractive forces between $0f_{7/2}$ protons and $0f_{5/2}$ neutrons [63], as indicated in Fig. 7 (right). One neutron removal cross sections from these isotopes corroborated the neutron shell closures [64, 65]. The large $E(2_1^+)$ in ^{52}Ar further confirmed the robustness of the $N = 34$ shell closure [66]. In contrast, ^{50}Ar shows spectroscopic evidence of moderate collectivity and oblate deformation [67–69]. Further intriguing results have been obtained along the neutron-rich Calcium isotopes, including the first spectroscopy of ^{56,58}Ca [70]. They are discussed within the current series of review [71].

With 28 protons and 50 neutrons, ^{78}Ni forms a canonical doubly magic nucleus. Its robustness is, however, put in doubt due to its reliance on two magic numbers formed by a large spin-orbit orbit splitting. At lower masses, ^{42}Si features a strongly deformed shape [61, 72, 73], marking the first direct evidence of spin-orbit shell closure break down. This raises the question of the structure of neutron-rich Ni isotopes, and in particular ^{78}Ni. A captivating single particle level crossing occurs for the neutron-rich Cu isotopes, where the $0f_{5/2}$ level falls below the $0p_{3/2}$ level between neutron number $N = 44$ and 46 [74]. This is seen as an indication for a reduction of the $Z = 28$ shell gap.

Significant efforts have been undertaken to experimentally access the area near ^{78}Ni to evaluate its doubly magic nature. It has been believed for a long time that the relative weakness of the double spin-orbit shell closures makes them susceptible to quenching. Furthermore, effective shell model calculations predict the onset of deformation at $N = 50$ for neutron-rich nuclei [75]. This leads the $N = 50$ shell closure to break down below $Z = 28$, where it merges with the $N = 40$ island of inversion [76]. For the latter, new data on $E(2_1^+)$ and $E(4_1^+)$ in ^{62}Ti, ^{66}Cr, and ^{70,72}Fe [77, 78] collected with SEASTAR substantiated its large extension. For ^{78}Ni itself, theoretical predictions features low-lying deformed intruder states. The first spectroscopy of ^{78}Ni confirmed this notion [79]. Its structure is discussed, together with neighboring nuclei, in the present series of reviews [80], including further details on the extend of the $N = 40$ Island of Inversion [81].

4.2. Shape Coexistence and Deformation

Neutron-rich isotopes between Ni and Sn feature a change from a spherical shape at $N = 50$ towards more collective configurations. However, this shift undergoes significant changes in steps, with a sudden break at neutron number $N = 60$. The sudden and quite dramatic onset of deformation for the Sr and Zr nuclei comes along with low-lying, deformed 0^+ states, becoming the ground state beyond $N = 60$, while the spherical 0^+ states become nonyrast. This shape coexistence of spherical and deformed configurations around $N = 60$ is subject to extensive contemporary research [82, 83]. A comprehensive description of the phenomenon can be found in Ref. [84], sometimes also referred to as type-II shell evolution in microscopic calculations [85].

While signatures for shape coexistence can be observed in ^{78}Ni [79], already the Zn isotopes' yrast structure is susceptible to the influence of a diminished $N = 50$ shell gap [86, 87]. Additional SEASTAR results indicate that Ge, Se, and Kr isotopes follow different deformation routes compared to their Sr and Zr counterparts [88–91]. Beyond mean field models generally predict this shape coexistence [92, 93], such as between prolate and oblate forms in Se isotopes around $N = 56$, leading to triaxiality ranging from soft to more rigid structures.

SEASTAR experiments reached medium mass nuclei as far as ^{110}Zr and ^{112}Mo [94], which tested the potential $Z = 40$, $N = 70$ harmonic oscillator shell gap. A comprehensive summary of all the observed nuclear structure phenomena in the neutron-rich Zn to Mo isotopes can be found within the present series of reviews [95].

4.3. Correlated Neutrons and Cluster Formation

Nuclei a exhibit spatially correlated substructures, such as α particles, i.e., strongly bound clusters of two protons and two neutrons, most prominently in the vicinity of the decay threshold [96], as initially pictured by the Ikeda diagram [97]. For instance, the Hoyle state in ^{12}C at 7.65 MeV, an excited 0^+ state lying just above the three-α threshold, is considered to be a loosely bound, spatially extended configuration of three α particles of immense importance in nuclear astrophysics [98, 99]. The Hoyle state manifests a classic example of a 3-α cluster state in the Ikeda diagram and exemplifies the relevance of cluster degrees of freedom, motivating contemporary efforts to explore similar configurations in heavier as well as exotic nuclei. How these cluster structures manifest themselves out of a mean field of nucleons remains an open topic in contemporary research. Experimentally, α-condensate states, 3-α-linear-chain states and molecular resonances have been observed in light isotopes [100–102] where an excess of neutrons may contribute in favoring the stability of such structures as electrons in covalent bonds in molecules. Still, owing to the experimental challenges, little is known on such molecular states in exotic nuclei.

Beyond α clustering, the role of neutron correlations in systems far off stability has recently drawn increasing attention. These correlations can manifest themselves in various forms. Two-neutron correlations are well known in the neutron-rich isotope ^{11}Li [103], but only recently their angular correlation and density-dependent distribution was established [104]. Beyond two-neutrons, the existence of bound or resonant states composed purely of three or four neutrons, often referred to as 'trineutron' or 'tetraneutron' states, has long been doubted in light of clear experimental evidence. Early indications of a tetraneutron resonance [105, 106] were suggestive but inconclusive. Only recently the existence of a free

correlated four neutron system could be observed [22]. It was populated from the quasifree scattering reaction ^{8}He$(P, p\alpha)$ and made possible through the high luminosity provided by a liquid hydrogen target. The nature of the correlations at the origin of the observation still need to be understood. Conversely, no trineutron resonance candidate has been observed to date [107]. A review within this series is dedicated to these intriguing phenomena of cluster formation and multi-neutron correlations [108].

4.4. The Neutron Dripline

The progression of the neutron drip line, which marks the limit of existence for neutron-rich nuclei, displays a regular pattern from light to medium-mass nuclei. However, a notable anomaly is observed in the oxygen isotopes. This irregularity is difficult to capture by shell-model calculations that utilize microscopic two-nucleon forces and it has been shown that the inclusion of three-body forces and continuum effects are necessary [109, 110]. These forces introduce repulsive effects among surplus neutrons, shifting the neutron drip line from the naturally assumed ^{28}O to the experimentally confirmed ^{24}O [111]. Predicting the neutron dripline from beyond oxygen in the Island of Inversion must necessarily include deformation. With the addition of neutrons, the nucleus undergoes increased ellipsoidal deformation, resulting in a considerable increase in binding energy [112]. The implications for the exact boundaries of the Island of Inversion are yet to be evaluated experimentally. Its southern shore is notoriously difficult to access. New breakthrough experiments, obtained mainly due to the enhanced luminosity obtained with MINOS, place the neutron-rich isotopes ^{26,27,28}O and $^{27\text{-}30}$F inside the Island of Inversion [113–117]. Further insights into this fascinating topic are explored in the current series of review articles [39].

Depending on its precise position, future facilities have the potential to reach the neutron drip line up to calcium isotopes, a topic currently under rigorous scientific discussion. Early *ab initio* computations suggested that ^{60}Ca was unbound [118], yet its existence was subsequently verified [119]. The boundaries of the nuclear landscape continue to be a prominent area of modern research. Different theoretical approaches, such as density functional theory [120] and *ab initio* methods [121], strive to offer a broader understanding including their respective uncertainties. In this context, the calcium isotopes have emerged as critical areas for rigorous examination of these models. With the spectroscopy of ^{56,58}Ca, further insight into the location of the dripline was obtained, discussed also within the current series of review articles [71, 81].

5. Perspectives

The period from the completion of the RIBF of RIKEN in 2007 to the present has marked a golden age for studying the structure of neutron-rich nuclei, driven by its world-class capabilities. New instruments such as the thick liquid hydrogen target MINOS combined with particle and γ detectors, alongside quasi-free secondary scattering reactions in inverse kinematics, have proven particularly effective. Over the time period MINOS stayed at RIKEN, three in-beam γ campaigns and four particle-spectroscopy experiments at SAMURAI have yielded remarkable scientific results, leading to over 40 publications. These include groundbreaking achievements, such as the first spectroscopy of the doubly magic nucleus ^{78}Ni [79], the discovery of a correlated free four-neutron system [22], and the first spectroscopy of the unbound nucleus ^{28}O [116].

This success is owed to those who envisioned and built the RIBF, resulting now in the obligation to inspire and support the next generation of nuclear physicists by exploring and creating new research avenues, a mission that is already in progress. The RIBF is well-positioned to play a leading role in the forthcoming developments in nuclear physics, with a particular focus on exploring even more exotic neutron-rich nuclei and advancing our understanding of nuclear structure and fundamental symmetries thanks to its planned upgrade that will yield up to 2 particle micro Ampere of ^{238}U primary beam [28]. Future enhancements to the RIBF's capabilities also include new detection technologies that will allow for more precise and detailed experiments, enabling discoveries that are currently beyond reach. New particle and γ spectroscopy devices, such as STRASSE [122], HYPATIA [123], and TOGAXSI [124], will further boost sensitivity, allowing researchers to push further the exploration of neutron-rich isotopes. A review in this series is dedicated to this topic [125]. Experimental efforts go hand in hand with a better theory. A better description of deformation and many-body excitations, covering the entire nuclear chart, is required improvements for nuclear structure models. Future experimental programs are calling for a better understanding of reaction mechanisms, not least solving the quenching issue [18], the role of the continuum, new structure approaches, and a better handle on the errors in predictions.

The RIBF's work is complemented by efforts at international in-flight separator facilities, such as FRIB in the United States, and in the future FAIR in Germany, HIAF in China, and RAON in Korea, all three currently under construction. Together, these institutions not only compete with each other, but also form a collaborative network, enabling shared discoveries and cross-validation of new findings. Through these upgrades and global networks, the RIBF is positioned to lead groundbreaking discoveries and to guide the next generation of nuclear scientists.

Acknowledgements. The achievements summarized in this review were made possible by international collaborations with exceptional commitment and expertise involving more than 100 scientists from more than 30 institutes. The scientific results would not have been possible without the extraordinary support of the RIKEN Nishina Center staff, chief scientists and NP-PAC members. Above all, a large part of the merit goes to the involved early-career researchers and their dedication to science. M.L. Cortes is thanked for providing adaptions of Figs. 4, 5, and 6, and O. Kamigaito is thanked for providing an adaption of Fig. 2. A. O. acknowledges the support from the European Research Council through the grant No. MINOS-258567, the Alexander von Humboldt foundation and the Deutsche Forschungsgemeinschaft (DFG, German Research Foundation) through the Project No. 279384907–SFB 1245. C.A.B. acknowledges support by the U.S. Department of Energy grant DE-FG02-08ER41533.

References

[1] M. Goeppert Mayer. On closed shells in nuclei. *Phys. Rev.*, 75:1969, 1949.
[2] O. Haxel, J.H.D. Jensen, and H.E. Suess. On the "magic numbers" in nuclear structure. *Phys. Rev.*, 75:1766, 1949.
[3] A. Obertelli, A. Delbart, S. Anvar, et al. MINOS: A vertex tracker coupled to a thick liquid-hydrogen target for in-beam spectroscopy of exotic nuclei. *Eur. Phys. J. A*, 50:8, 2014.
[4] Th.A.J. Maris, Peter Hillman, and H. Tyrén. Quasi-elastic scattering and nuclear structure. *Nuclear Physics*, 7:1–9, 1958.
[5] H. Tyrén, Peter Hillman, and Th.A.J. Maris. High energy (p, 2p) reactions and proton binding

energies. *Nuclear Physics*, 7:10–23, 1958.
[6] Gerhard Jacob and Th. A. J. Maris. Quasi-free scattering and nuclear structure. *Rev. Mod. Phys.*, 38:121–142, 1966.
[7] N. S. Chant and P. G. Roos. Distorted-wave impulse-approximation calculations for quasifree cluster knockout reactions. *Phys. Rev. C*, 15:57–68, 1977.
[8] Daphne F. Jackson. *The Investigation of Hole States in Nuclei by Means of Knockout and Related Reactions*, pages 1–60. Springer US, Boston, MA, 1971.
[9] P. Kitching, C.A. Miller, W.C. Olsen, et al. Quasi-free scattering of polarized protons. *Nucl. Phys. A*, 340(2):423–444, 1980.
[10] C. W. Wang, N. S. Chant, P. G. Roos, et al. Quasi-free (α,2α) reaction induced by 140 MeV alpha particles on ^{9}Be, ^{12}C, ^{16}O, and ^{20}Ne. *Phys. Rev. C*, 21:1705–1717, 1980.
[11] P. G. Roos, N. S. Chant, A. A. Cowley, et al. Absolute spectroscopic factors from the $(p, p\alpha)$ reaction at 100 MeV on 1p-shell nuclei. *Phys. Rev. C*, 15:69–83, 1977.
[12] Arun K. Jain and Bhushan N. Joshi. Finite range effects in (α, 2α) reactions. *Phys. Rev. Lett.*, 103:132503, 2009.
[13] Y. Yasuda, H. Sakaguchi, S. Asaji, et al. Spectroscopic factors and strength distributions for the deeply bound orbitals in ^{40}Ca obtained from the $(\tilde{\text{p}}, 2\text{p})$ reaction at 392 MeV. *Phys. Rev. C*, 81:044315, 2010.
[14] Yoshiteru Kudo and Hitoshi Tsunoda. Spin observables of proton knockout reaction and effective nucleon-nucleon interaction. *Progr. of Theor. Phys.*, 89(1):89–101, 1993.
[15] B. N. Joshi, M. Kushwaha, and Arun K. Jain. On the discrepancy between proton and α-induced d-cluster knockout on 16o. *Prog. Theor. Exp. Phys.*, 2016(12):121D01, 2016.
[16] G. F. Steyn, S. V. Förtsch, A. A. Cowley, et al. α-clustering probabilities extracted from the $^{12}\text{C}(\alpha, 2\alpha)^{8}\text{Be}$ reaction at 200 MeV. *Phys. Rev. C*, 59:2097–2102, 1999.
[17] T. Wakasa, K. Ogata, and T. Noro. Proton-induced knockout reactions with polarized and unpolarized beams. *Progress in Particle and Nuclear Physics*, 96:32–87, 2017.
[18] T. Aumann, C. Barbieri, D. Bazin, et al. Quenching of single-particle strength from direct reactions with stable and rare-isotope beams. *Prog. Part. Nucl. Phys.*, 118:103847, 2021.
[19] Kazuyuki Ogata, Kazuki Yoshida, and Yoshiki Chazono. pikoe: A computer program for distorted-wave impulse approximation calculation for proton induced nucleon knockout reactions. *Computer Physics Communications*, 297:109058, 2024.
[20] T. Aumann, C. A. Bertulani, and J. Ryckebusch. Quasifree (p,2p) and (p,pn) reactions with unstable nuclei. *Phys. Rev. C*, 88:064610, 2013.
[21] V. Panin et al. Exclusive measurements of quasi-free proton scattering reactions in inverse and complete kinematics. *Phys. Lett. B*, 753:204–210, 2016.
[22] M. Duer, T. Aumann, R. Gernhäuser, et al. Observation of a correlated free four-neutron system. *Nature*, 606(7915):678–682, 2022.
[23] C. A. Bertulani, A. Idini, and C. Barbieri. Examination of the sensitivity of quasifree reactions to details of the bound-state overlap functions. *Phys. Rev. C*, 104:L061602, 2021.
[24] Jianguo Li, Carlos A. Bertulani, and Furong Xu. Nuclear spectroscopy with heavy ion nucleon knockout and (p,2p) reactions. *Phys. Rev. C*, 105:024613, 2022.
[25] Yasushige Yano. The RIKEN RI Beam Factory project: A status report. *Nucl. Instrum. Methods Phys. Res. B*, 261:1009–1013, 2007.
[26] H. Okuno et al. The Superconducting Ring Cyclotron in RIKEN. *IEEE Trans. Applied*, 261:1009, 2007.
[27] T. Kubo et al. BigRIPS separator and ZeroDegree spectrometer at RIKEN RI Beam Factory. *Prog. Theor. Exp. Phys.*, 2012:03C003, 2012.
[28] RIBF Facility Upgrade Project. `https://www.nishina.riken.jp/researcher/RIBFupgrade/RIBF_Upgrade_NCAC.pdf`, 2024.
[29] RIKEN Accelerator Progress Report 2021. `https://www.nishina.riken.jp/researcher/APR/APR055/pdf/RIKEN_APR55.pdf`, 2024.
[30] T. Ohnishi. Practical Use of High-Temperature Oven for 28 GHz Superconducting ECR Ion Source at RIKEN. *Proc. ECRIS'18, Catania, Italy*, page 180, 2018.
[31] O. Kamigaito et al. Design of New Injector to RIKEN Ring Cyclotron. *Proc. 3rd PASJ and 31st LAM in Japan, Sendai, Aug. 2006, paper WP78*, page 502, 2006.
[32] H. Imao. Development of gas stripper at RIBF. *Proc. IPAC'18, Vancouver, Canada*, page 41, 2018.
[33] K. Yamada et al. Upgrade and current status of high-frequency systems for RIKEN Ring Cyclotron. *Proc. 23rd Int. Conf. on Cyclotrons and their Applications (Cyclotrons'22), Beijing, China*, 2022.
[34] N. Fukuda, T. Kubo, T. Ohnishi, et al. Identification and separation of radioactive isotope beams by the BigRIPS separator at the RIKEN RI Beam Factory. *Nucl. Instrum. Methods Phys. Res. B*, 317:323–332, 2013. XVIth International Conference on ElectroMagnetic Isotope Separators and

Techniques Related to their Applications, December 2–7, 2012 at Matsue, Japan.
[35] H. Kumagai et al. Delay-line PPAC for high-energy light ions. *Nucl. Instrum. Methods Phys. Res. A*, 470(3):562, 2001.
[36] K. Kimura et al. High-rate particle identification of high-energy heavy ions using a tilted electrode gas ionization chamber. *Nucl. Instrum. Methods Phys. Res. A*, 538:607, 2005.
[37] S. Takeuchi, T. Motobayashi, Y. Togano, et al. DALI2: A NaI(Tl) detector array for measurements of γ rays from fast nuclei. *Nucl. Instrum. Methods Phys. Res. A*, 763:596, 2014.
[38] T. Kobayashi, N. Chiga, T. Isobe, et al. SAMURAI spectrometer for RI beam experiments. *Nucl. Instrum. Methods Phys. Res. B*, 317:294, 2013.
[39] J. Kahlbow. The southern shore of the Island of Inversion studied via quasi-free scattering. *Prog. Theor. Exp. Phys*, 2025.
[40] M.L. Cortes. *Inelastic scattering of Ni and Zn isotopes off a proton target.* PhD thesis, TU Darmstadt, 2016.
[41] K. Boretzky, I. Gašparić, M. Heil, et al. NeuLAND: The high-resolution neutron time-of-flight spectrometer for R3B at FAIR. *Nucl. Instrum. Methods Phys. Res. A*, 1014:165701, 2021.
[42] T. Nakamura and Y. Kondo. Large acceptance spectrometers for invariant mass spectroscopy of exotic nuclei and future developments. *Nucl. Instrum. Methods Phys. Res. B*, 376:156–161, 2016. Proceedings of the XVIIth International Conference on Electromagnetic Isotope Separators and Related Topics (EMIS2015), Grand Rapids, MI, U.S.A., 11-15 May 2015.
[43] P. Doornenbal. In-beam gamma-ray spectroscopy at the RIBF. *Prog. Theor. Exp. Phys.*, 2012:03C004, 2012.
[44] I. Murray et al. DALI2^{+} at the RIKEN Nishina Center RIBF. *RIKEN Acce. Prog. Rep.*, 51:158, 2018.
[45] A. Obertelli and T. Uesaka. Hydrogen targets for exotic-nuclei studies developed over the past 10 years. *Eur.Phys. J. A*, 47(9):105, 2011.
[46] C. Louchart, J.M. Gheller, Ph. Chesny, et al. The prespec liquid-hydrogen target for in-beam gamma spectroscopy of exotic nuclei at GSI. *Nucl. Instrum. Methods Phys. Res. A*, 736:81–87, 2014.
[47] Y. Giomataris, Ph. Rebourgeard, J.P. Robert, and G. Charpak. MICROMEGAS: A high-granularity position-sensitive gaseous detector for high particle-flux environments. *Nucl. Instrum. Methods Phys. Res. A*, 376(1):29 – 35, 1996.
[48] I. Giomataris, R. De Oliveira, S. Andriamonje, et al. Micromegas in a bulk. *Nucl. Instrum. Methods Phys. Res. A*, 560(2):405 – 408, 2006.
[49] C. Santamaria et al. Tracking with the MINOS Time Projection Chamber. *Nucl. Instrum. Methods Phys. Res. A*, 905:138–148, 2018.
[50] D. Calvet. A versatile readout system for small to medium scale gaseous and silicon detectors. *IEEE Transactions on Nuclear Science*, 61(1):675 – 682, 2014. Cited by: 32.
[51] P. Baron, D. Calvet, F. Château, et al. Operational Experience With the Readout System of the MINOS Vertex Tracker. *IEEE Transactions on Nuclear Science*, 64(6):1494 – 1500, 2017.
[52] C. Thibault, R. Klapisch, C. Rigaud, et al. Direct measurement of the masses of ^{11}Li and $^{26-32}$Na with an on-line mass spectrometer. *Phys. Rev. C*, 12:644, 1975.
[53] X. Campi, H. Flocard, A.K. Kerman, and S. Koonin. Shape transition in the neutron rich sodium isotopes. *Nucl. Phys. A*, 251:193, 1975.
[54] C. Détraz, D. Guillemaud, G. Huber, et al. Beta decay of $^{27-32}$Na and their descendants. *Phys. Rev. C*, 19:164, 1979.
[55] T. Motobayashi, Y. Ikeda, K. Ieki, et al. Large deformation of the very neutron-rich nucleus ^{32}Mg from intermediate-energy Coulomb excitation. *Phys. Lett. B*, 346:9, 1995.
[56] E. K. Warburton, J. A. Becker, and B. A. Brown. Mass systematics for A=29–44 nuclei: The deformed A$\sim$32 region. *Phys. Rev. C*, 41:1147, 1990.
[57] P. Doornenbal, H. Scheit, S. Takeuchi, et al. In-Beam γ-Ray Spectroscopy of ^{34,36,38}Mg: Merging the N=20 and N=28 Shell Quenching. *Phys. Rev. Lett.*, 111:212502, 2013.
[58] E. Caurier, F. Nowacki, and A. Poves. Merging of the islands of inversion at $N = 20$ and $N = 28$. *Phys. Rev. C*, 90:014302, 2014.
[59] T Otsuka and Y Tsunoda. The role of shell evolution in shape coexistence. *J. Phys. G*, 43(2):024009, 2016.
[60] P. Doornenbal, H. Scheit, N. Aoi, et al. Spectroscopy of ^{32}Ne and the "Island of Inversion". *Phys. Rev. Lett.*, 103:032501, 2009.
[61] S. Takeuchi, M. Matsushita, N. Aoi, et al. Well developed deformation in ^{42}Si. *Phys. Rev. Lett.*, 109:182501, 2012.
[62] D. Steppenbeck, S. Takeuchi, N. Aoi, et al. Evidence for a new nuclear 'magic number' from the level structure of ^{54}Ca. *Nature*, 502:207, 2013.
[63] T. Otsuka, T. Suzuki, R. Fujimoto, et al. Evolution of nuclear shells due to the tensor force. *Phys. Rev. Lett.*, 95:232502, 2005.

[64] S. Chen, J. Lee, P. Doornenbal, et al. Quasifree Neutron Knockout from ^{54}Ca Corroborates Arising $N = 34$ Neutron Magic Number. *Phys. Rev. Lett.*, 123:142501, 2019.

[65] M. Enciu et al. Extended $p_{3/2}$ Neutron Orbital and the $N = 32$ Shell Closure in ^{52}Ca. *Phys. Rev. Lett.*, 129:262501, 2022.

[66] H. N. Liu, A. Obertelli, P. Doornenbal, et al. How Robust is the $N = 34$ Subshell Closure? First Spectroscopy of ^{52}Ar. *Phys. Rev. Lett.*, 122:072502, 2019.

[67] D. Steppenbeck, S. Takeuchi, N. Aoi, et al. Low-lying structure of ^{50}Ar and the $N = 32$ subshell closure. *Phys. Rev. Lett.*, 114:252501, 2015.

[68] M. L. Cortés, W. Rodriguez, P. Doornenbal, et al. $N = 32$ shell closure below calcium: Low-lying structure of ^{50}Ar. *Phys. Rev. C*, 102:064320, 2020.

[69] B. D. Linh, A. Corsi, A. Gillibert, et al. Onset of collectivity for argon isotopes close to $N = 32$. *Phys. Rev. C*, 109:034312, 2024.

[70] S. Chen et al. Level structures of ^{56,58}Ca cast doubt on a doubly magic ^{60}Ca. *Phys. Lett. B*, 843:138025, 2023.

[71] H. Liu, S. Chen, and F. Browne. Shell Migration at N = 32, 34 around Ca Region. *Prog. Theor. Exp. Phys*, 2025.

[72] B. Bastin, S. Grévy, D. Sohler, et al. Collapse of the $N = 28$ Shell Closure in ^{42}Si. *Phys. Rev. Lett.*, 99:022503, 2007.

[73] A. Gade, B. A. Brown, J. A. Tostevin, et al. Is the Structure of ^{42}Si Understood? *Phys. Rev. Lett.*, 122:222501, 2019.

[74] K. T. Flanagan, P. Vingerhoets, M. Avgoulea, et al. Nuclear Spins and Magnetic Moments of ^{71,73,75}Cu: Inversion of $\pi 2p_{3/2}$ and $\pi 1f_{5/2}$ Levels in ^{75}Cu. *Phys. Rev. Lett.*, 103:142501, 2009.

[75] F. Nowacki, A. Poves, E. Caurier, and B. Bounthong. Shape coexistence in ^{78}Ni as the portal to the fifth island of inversion. *Phys. Rev. Lett.*, 117:272501, 2016.

[76] S. M. Lenzi, F. Nowacki, A. Poves, and K. Sieja. Island of inversion around ^{64}Cr. *Phys. Rev. C*, 82:054301, 2010.

[77] C. Santamaria, C. Louchart, A. Obertelli, et al. Extension of the $N = 40$ Island of Inversion towards $N = 50$: Spectroscopy of ^{66}Cr, ^{70,72}Fe. *Phys. Rev. Lett.*, 115:192501, 2015.

[78] M.L. Cortés, W. Rodriguez, P. Doornenbal, et al. Shell evolution of N = 40 isotones towards ^{60}Ca: First spectroscopy of ^{62}Ti. *Phys. Lett. B*, 800:135071, 2020.

[79] R. Taniuchi, C. Santamaria, P. Doornenbal, et al. ^{78}Ni revealed as a doubly magic stronghold against nuclear deformation. *Nature*, 569:53, 2019.

[80] R. Taniuchi. Competition of the shell closure and deformations across the doubly magic ^{78}Ni. *Prog. Theor. Exp. Phys*, 2025.

[81] M.L. Cortés. The Island of Inversion at $N = 40$. *Prog. Theor. Exp. Phys*, 2025.

[82] E. Clément, M. Zielińska, A. Görgen, et al. Spectroscopic Quadrupole Moments in ^{96,98}Sr: Evidence for Shape Coexistence in Neutron-Rich Strontium Isotopes at $N = 60$. *Phys. Rev. Lett.*, 116:022701, 2016.

[83] T. Togashi, Y. Tsunoda, T. Otsuka, and N. Shimizu. Quantum phase transition in the shape of Zr isotopes. *Phys. Rev. Lett.*, 117:172502, 2016.

[84] K. Heyde and J. L. Wood. Shape coexistence in atomic nuclei. *Rev. Mod. Phys.*, 83:1467, 2011.

[85] Y. Tsunoda, T. Otsuka, N. Shimizu, et al. Novel shape evolution in exotic Ni isotopes and configuration-dependent shell structure. *Phys. Rev. C*, 89:031301, 2014.

[86] Y. Shiga, K. Yoneda, D. Steppenbeck, et al. Investigating nuclear shell structure in the vicinity of ^{78}Ni: Low-lying excited states in the neutron-rich isotopes ^{80,82}Zn. *Phys. Rev. C*, 93:024320, 2016.

[87] C.M. Shand, Zs. Podolyák, M. Górska, et al. Shell evolution beyond Z=28 and N=50: Spectroscopy of ^{81,82,83,84}Zn. *Phys. Lett. B*, 773:492, 2017.

[88] M. Lettmann, V. Werner, N. Pietralla, et al. Triaxiality of neutron-rich ^{84,86,88}Ge from low-energy nuclear spectra. *Phys. Rev. C*, 96:011301, 2017.

[89] S. Chen, P. Doornenbal, A. Obertelli, et al. Low-lying structure and shape evolution in neutron-rich Se isotopes. *Phys. Rev. C*, 95:041302, 2017.

[90] F. Flavigny, P. Doornenbal, A. Obertelli, et al. Shape Evolution in Neutron-Rich Krypton Isotopes Beyond $N = 60$: First Spectroscopy of ^{98,100}Kr. *Phys. Rev. Lett.*, 118:242501, 2017.

[91] R.-B. Gerst, A. Blazhev, K. Moschner, et al. γ-ray spectroscopy of low-lying yrast and non-yrast states in neutron-rich ^{94,95,96}Kr. *Phys. Rev. C*, 105:024302, 2022.

[92] J. P. Delaroche, M. Girod, J. Libert, et al. Structure of even-even nuclei using a mapped collective Hamiltonian and the D1S Gogny interaction. *Phys. Rev. C*, 81:014303, 2010.

[93] Tomás R. Rodríguez. Structure of krypton isotopes calculated with symmetry-conserving configuration-mixing methods. *Phys. Rev. C*, 90:034306, 2014.

[94] N. Paul, A. Corsi, A. Obertelli, et al. Are There Signatures of Harmonic Oscillator Shells Far from

Stability? First Spectroscopy of ^{110}Zr. *Phys. Rev. Lett.*, 118:032501, 2017.
[95] S. Chen, F. Browne, T. Rodríguez, and V. Werner. Deformation from zinc to zirconium. *Prog. Theor. Exp. Phys*, 2025.
[96] J. P. Ebran, E. Khan, T. Nikšić, and D. Vretenar. How atomic nuclei cluster. *Nature*, 487(7407):341–344, 2012.
[97] Kiyomi Ikeda, Noboru Takigawa, and Hisashi Horiuchi. The systematic structure-change into the molecule-like structures in the self-conjugate 4n nuclei. *Progr. of Theor. Phys. Suppl.*, E68:464–475, 1968.
[98] F. Hoyle. On nuclear reactions occurring in very hot stars. i. the synthesis of elements from carbon to nickel. *Astrophysical Journal Supplement Series*, 1:12, 1954.
[99] M. Freer and H.O.U. Fynbo. The hoyle state in ^{12}C. *Prog. Part. Nucl. Phys.*, 78:1–23, 2014.
[100] M. Freer, E. Casarejos, L. Achouri, et al. $\alpha : 2n : \alpha$ molecular band in ^{10}Be. *Phys. Rev. Lett.*, 96:042501, 2006.
[101] Z. H. Yang, Y. L. Ye, Z. H. Li, et al. Observation of enhanced monopole strength and clustering in ^{12}Be. *Phys. Rev. Lett.*, 112:162501, 2014.
[102] Y. Liu, Y. L. Ye, J. L. Lou, et al. Positive-parity linear-chain molecular band in ^{16}C. *Phys. Rev. Lett.*, 124:192501, 2020.
[103] T. Nakamura, A. M. Vinodkumar, T. Sugimoto, et al. Observation of strong low-lying $E1$ strength in the two-neutron halo nucleus ^{11}Li. *Phys. Rev. Lett.*, 96:252502, 2006.
[104] Y. Kubota, A. Corsi, G. Authelet, et al. Surface localization of the dineutron in ^{11}Li. *Phys. Rev. Lett.*, 125:252501, 2020.
[105] F. M. Marqués, M. Labiche, N. A. Orr, et al. Detection of neutron clusters. *Phys. Rev. C*, 65:044006, 2002.
[106] K. Kisamori, S. Shimoura, H. Miya, et al. Candidate resonant tetraneutron state populated by the ^{4}He(^{8}He,^{8} Be) reaction. *Phys. Rev. Lett.*, 116:052501, 2016.
[107] K. Miki, K. Kameya, D. Sakai, et al. Precise spectroscopy of the $3n$ and $3p$ systems via the ^{3}H(t, ^{3}He)$3n$ and ^{3}He(^{3}He, t)$3p$ reactions at intermediate energies. *Phys. Rev. Lett.*, 133:012501, 2024.
[108] Z. Yang and Y. Kubota. Neutron correlations and clustering in neutron-rich nuclear systems. *Prog. Theor. Exp. Phys*, 2025.
[109] Takaharu Otsuka, Toshio Suzuki, Jason D. Holt, et al. Three-body forces and the limit of oxygen isotopes. *Phys. Rev. Lett.*, 105:032501, 2010.
[110] G. Hagen, M. Hjorth-Jensen, G. R. Jansen, et al. Continuum effects and three-nucleon forces in neutron-rich oxygen isotopes. *Phys. Rev. Lett.*, 108:242501, 2012.
[111] H. Sakurai, S.M. Lukyanov, M. Notani, et al. Evidence for particle stability of ^{31}F and particle instability of ^{25}N and ^{28}O. *Phys. Lett. B*, 448:180, 1999.
[112] N. Tsunoda, T. Otsuka, K. Takayanagi, et al. The impact of nuclear shape on the emergence of the neutron dripline. *Nature*, 587:66, 2020.
[113] Y. Kondo, T. Nakamura, R. Tanaka, et al. Nucleus ^{26}O: A barely unbound system beyond the drip line. *Phys. Rev. Lett.*, 116:102503, 2016.
[114] P. Doornenbal, H. Scheit, S. Takeuchi, et al. Low-Z shore of the "island of inversion" and the reduced neutron magicity toward ^{28}O. *Phys. Rev. C*, 95:041301, 2017.
[115] A. Revel, O. Sorlin, F. M. Marqués, et al. Extending the southern shore of the island of inversion to ^{28}F. *Phys. Rev. Lett.*, 124:152502, 2020.
[116] Y. Kondo et al. First observation of ^{28}O. *Nature*, 620:965, 2023.
[117] J. Kahlbow, T. Aumann, O. Sorlin, et al. Magicity versus superfluidity around ^{28}O viewed from the study of ^{30}F. *Phys. Rev. Lett.*, 133:082501, 2024.
[118] G. Hagen, M. Hjorth-Jensen, G. R. Jansen, et al. Evolution of shell structure in neutron-rich calcium isotopes. *Phys. Rev. Lett.*, 109:032502, 2012.
[119] O. B. Tarasov, D. S. Ahn, D. Bazin, et al. Discovery of ^{60}Ca and Implications For the Stability of ^{70}Ca. *Phys. Rev. Lett.*, 121:022501, 2018.
[120] J. Erler et al. The limits of the nuclear landscape. *Nature*, 486:509, 2012.
[121] S. R. Stroberg, J. D. Holt, A. Schwenk, and J. Simonis. Ab initio limits of atomic nuclei. *Phys. Rev. Lett.*, 126:022501, 2021.
[122] H. N. Liu, F. Flavigny, H. Baba, et al. STRASSE: A silicon tracker for quasi-free scattering measurements at the RIBF. *The Eur. Phys. J. A*, 59(6):121, 2023.
[123] HYPATIA array. `https://www.nishina.riken.jp/collaboration/SUNFLOWER/devices/hypatia/index.php`, 2024.
[124] J. Tanaka, R. Tsuji, K. Higuchi, et al. Designing TOGAXSI: Telescope for inverse-kinematics cluster-knockout reactions. *Nucl. Instrum. Methods Phys. Res. B*, 542:4–6, 2023.

[125] J. Tanaka, M.L. Cortés, H. Liu, and R. Taniuchi. Detectors for next-generation quasi-free scattering experiments. *Prog. Theor. Exp. Phys*, 2025.